Femtosecond laser processing of quartz wafers for precision cutting of tuning forks

Journal of Physics: Photonics

OPEN ACCESS

RECEIVED
4 November 2025

REVISED
28 December 2025

ACCEPTED FOR PUBLICATION
7 January 2026

PUBLISHED
16 January 2026

PAPER

Femtosecond laser processing of quartz wafers for precision cutting of tuning forks

Raffaele De Palo[1,*], **Jaka Mur**[2], **Matevž Marš**[2], **Felice Alberto Sfregola**[1,3], **Pietro Patimisco**[1,4], **Vincenzo Spagnolo**[1,4], **Antonio Ancona**[1,3], **Rok Petkovšek**[2] **and Annalisa Volpe**[1,3]

[1] Dipartimento Interuniversitario di Fisica, Polytechnic of Bari & University of Bari, Via G. Amendola 173, Bari 70125, Italy
[2] FOLAS LAB, Faculty of Mechanical Engineering, University of Ljubljana, Aškerčeva cesta 6, 1000 Ljubljana, Slovenia
[3] National Research Council of Italy, Institute for Photonics and Nanotechnologies, Via G. Amendola 173, Bari 70125, Italy
[4] PolySense Innovations srl, Via Amendola 173, Bari 70126, Italy
[*] Author to whom any correspondence should be addressed.

E-mail: raffaele.depalo@poliba.it

Keywords: femtosecond laser cutting, quartz micro-resonators, rapid-prototyping, eco-friendly fabrication

Supplementary material for this article is available online

Abstract

In this work, femtosecond laser cutting of quartz wafers was demonstrated as an environmentally friendly alternative to the standard etching methods for production of sensitive sensor devices. The proposed approach employed milling channels for processing of the entire wafer thickness. The laser parameters examined for this procedure were the pulse energy, the number of scans and the channel width. Subsequent analysis of each channel focused on evaluating its depth, the angle of tapering, and the overall quality of the cut. The laser system operated at a central wavelength of 515 nm, delivering pulses with a temporal width of 390 femtoseconds. After identifying the optimal laser parameters for achieving the best channel quality through the wafer thickness (280 μm), the method was used to directly laser-cut quartz microresonators in a tuning-fork geometry. The resonant performance of laser-cut tuning forks was simulated and experimentally validated using a laser-vibrometer under photoacoustic excitation. The results matched standard quartz-tuning-fork behavior, with the junction quality between the body and prongs significantly impacting performance. This study confirms femtosecond laser cutting as an efficient, eco-friendly method for producing quartz micro-devices, enabling single prototype fabrication not achievable with conventional methods.

1. Introduction

Quartz is one of the most exploited crystalline materials in many industrial fields, from glass making to watchmaking, because of its relative abundance on earth crust and of its properties: transparency from the UV to MID-IR, high melting point (1600 °C), chemical stability and thermo-piezoelectricity [1–5]. The latter property has favored, in the last 20 years, the development of advanced sensing applications employing quartz-based microresonators, such as quartz-tuning-forks (QTFs) and quartz-crystal-microbalances [6, 7]. QTFs have been widely employed as detectors in advanced spectroscopic techniques for gas sensing. In particular, in quartz-enhanced-Photoacoustic-spectroscopy (QEPAS) the QTF is used as sound detector, whereas it acts as photodetector in light-enhanced-photoacoustic-spectroscopy [8]. Both these optical techniques have hugely benefited from the development of customized QTFs based on different geometries and designs, properly tailored to answer various experimental issues and needs [9]. Beyond sensing, quartz-based resonant structures have also been investigated in advanced photonic systems operating under tailored symmetry conditions, such as PT-symmetric configurations, where super-resonant optical interactions can be engineered [10].

Photolithographic-assisted etching (PAE) and deep reactive ion etching (DRIE) are the standard methods for the production of QTFs any quartz-based device [11]. PAE relies on the wet etching of

quartz wafers, where an etching mask is applied using photolithography. At this stage, the substrates undergo chemical treatment in a etching solution composed of hydrofluoric acid and ammonium fluoride (NH_4F). Although this method is well-suited for the mass production of identical devices, it is less suitable for prototyping during preliminary laboratory testing due to the high cost and rigid requirements of the etching mask. Additionally, the use of toxic agents raises significant environmental concerns [12, 13]. Conversely, DRIE employs high-energy ion plasma treatment instead of chemical etching. With this method, a quartz wafer is coated with a non-reactive masking layer to define the QTF geometry, which is then etched within a gas chamber containing a high-density plasma with an optimized gas mixture. However, similar to PAE, the reliance on masking layers reduces the method's flexibility during prototyping, making it more suited for large-scale production. Thus, while both methods are firmly established and have been incorporated into industrial manufacturing lines, allowing for time- and cost-effective large-scale production of quartz-based devices, they simultaneously impose significant limitations on foundational research into the intrinsic properties and innovative designs of QTFs.

An increasingly appealing technique, valued for its flexibility and environmental sustainability, is ultra-short-pulsed-laser (USPL) technology. This approach eliminates the need for preliminary chemical treatments or costly lithographic masking, enabling highly localized material processing with micrometer-scale spatial resolution through precise laser beam focusing. Moreover, it delivers significantly superior processing quality compared to nano- and picosecond laser pulses [14].

In the last 30 years [15], USPL has been used in numerous applications, including alteration of the mechanical properties of surfaces [16, 17], fabrication of microdevices and alteration of photoactive media [18–20]. By employing pulses with durations of hundreds of femtoseconds (fs) and energies of few tens of μJ, USPL allows for easy machining and processing of ceramic composites [21] and of transparent dielectric, as glass, sapphire and quartz [22–24]. The latter are notoriously challenging to process due to their chemical inertness, hardness and brittleness [25]. When employing fs-pulses, the physical processes driving material modifications such as ablation [26–29], laser surface and refractive index modification [30, 31], are non-linear and much faster than any thermal mechanism, thus reducing likelihood of micro-cracks and defects caused by thermal effects [14, 25, 32].

The versatility of USPL technologies has facilitated the development of various approaches for direct laser-cutting of transparent dielectrics. Among these, stealth dicing and beam shaping are the most used methods on brittle materials like glass or sapphire [33–37]. However, there are still few works reporting on the cutting process of quartz crystals. Gaudiuso *et al* [38] reported on a stealth dicing method for cutting 250 μm thick quartz wafers. Similarly, Wang *et al* [39, 40] applied stealth dicing to 400 μm thick quartz wafers exploiting laser beam filamentation induced by non-linear effects. Stealth dicing relies on cleaving along laser-induced modifications, making it effective for straight-line processing. While it delivers excellent results in terms of processing depth, its primary limitation is its inability to accommodate complex patterns, particularly those involving corners. A reliable alternative involves cutting quartz wafers by ablating the entire crystal thickness using conventional Gaussian beams, enabling precise processing of complex geometries.

This study presents a method for directly cutting complex shapes from quartz wafers using laser ablation. A CPA hybrid femtosecond laser system with a central emission wavelength of 515 nm was employed, with the beam focused through a conventional F-theta lens to create a Gaussian beam profile. This approach delivered higher fluences and reduced processing times compared to more complex beam-shaping methods. Full wafer-thickness ablation was achieved by milling channels around the desired shape. The method was characterized by milled depth, taper angle, and cutting-edge quality before being applied to directly cut 280 μm thick quartz wafers into QTFs. The resonant properties of the laser-cut QTFs were simulated using finite element analysis (FEA) and validated through experimental vibrometric measurements, confirming the effectiveness of USPL processing for producing customized quartz resonators.

2. Materials and methods

Z-cut quartz wafers with dual-side polishing were employed in this study. The substrates, supplied by nano quartz wafer GmbH, had lateral dimensions of 25 $\times$ 25 mm^2 and a thickness of 280 μm. A wafer thickness of 280 μm was selected because it falls within the typical thickness range of QTFs fabricated with standard chemical etching methods. Laser processing was carried out using an open-table micromachining platform specifically configured for ultrafast laser applications figure 1.

The irradiation source was a femtosecond laser system based on a fiber chirped-pulse-amplification architecture, seeded by a mode-locked oscillator operating at 30 MHz [41, 42]. Pulse-on-demand operation was achieved through the injection of an auxiliary seeding diode within the amplification chain.

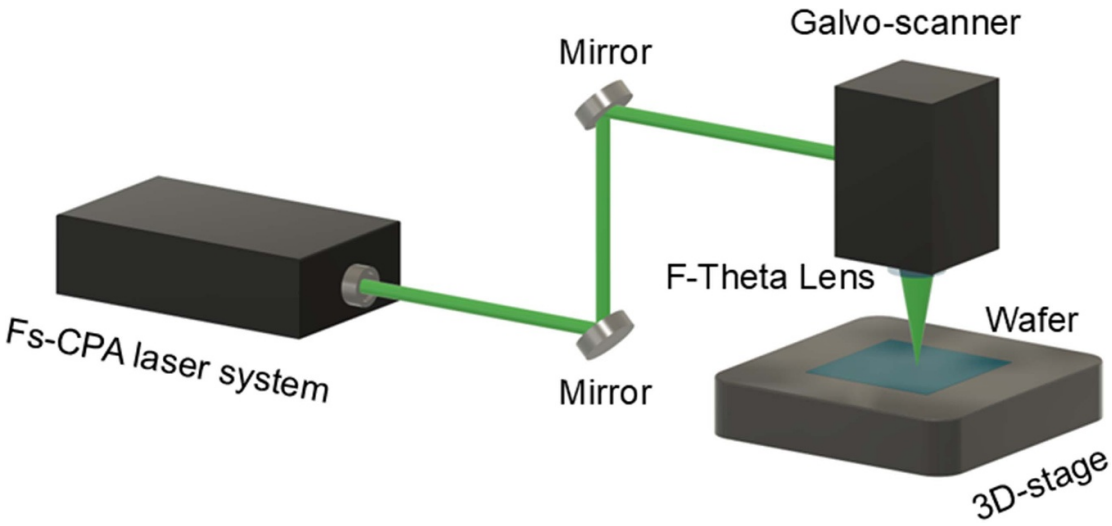

Figure 1. Layout of the femtosecond-laser-based optical system implemented for cutting of quartz substrates.

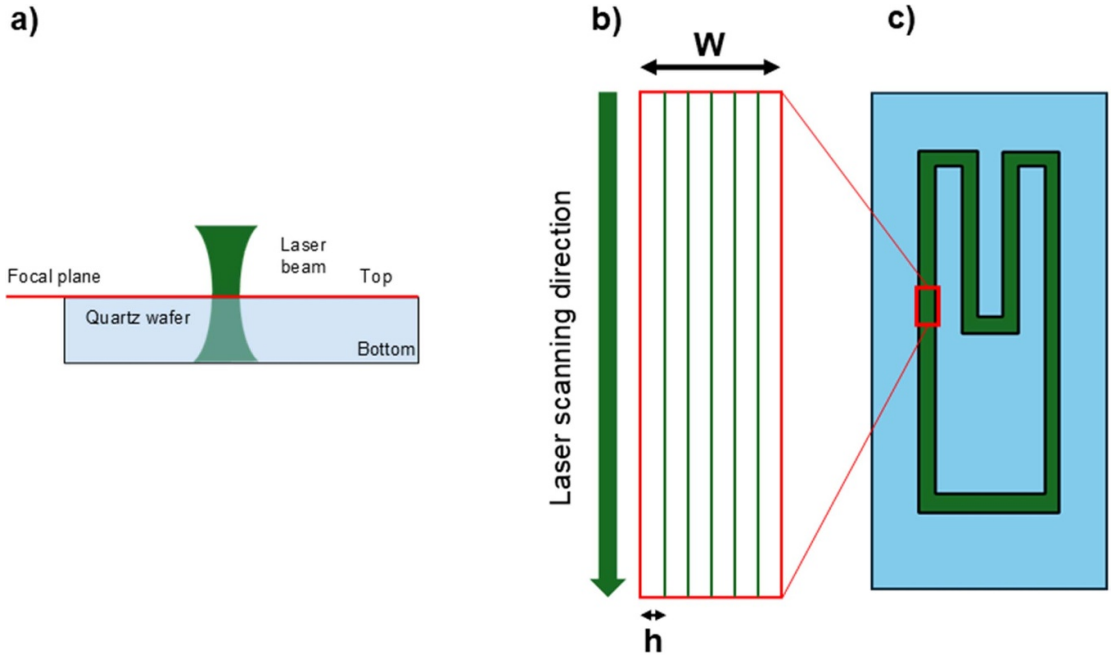

Figure 2. (a) Diagram illustrating the top-down fabrication strategy; (b) representation of a milling channel defined by width W and a vertical hatch pattern with step size h; (c) quartz wafer featuring a typical QTF geometry, surrounded by the corresponding milling contour (highlighted in green).

After amplification, the output radiation was frequency-doubled to 515 nm, providing pulse energies up to 35 μJ. During the experiments, the laser was operated at a repetition rate of 100 kHz, with a pulse duration set to 390 fs. The beam exhibited near-Gaussian spatial characteristics ($M^2 \sim 1.1$) and was delivered to the sample through an x–y galvanometric scanner and focused by an f-theta lens. Under these conditions, scanning velocities up to 4 m s^{-1} were achievable, and the resulting focal spot diameter (1 e^{-2}) was estimated to be 16 $\pm$ 1 μm. Sample positioning and alignment were ensured by a motorized three-axis translation stage.

The quartz wafers were processed employing a top–down approach combined with a milling channel strategy. This method is schematically represented in figure 2 (a).

Material structuring was performed using a surface-initiated laser ablation scheme, in which the laser beam interacts with the sample from the top side and progressively removes material through repeated scans along a predefined trajectory [22, 43]. In this approach, the target depth is reached through multiple iterations of the same scan path, without modifying the focal position during processing.

Table 1. Sets of parameters for the characterization of the milling channel.

F [J cm^{-2}]	N	PPS	W [μm]
4.7	100–200–300–400–500–600–700	3–2–1.5–1.2–1.0–0.9	100, 150, 200, 250, 300
5.7	50–100–150–200–250–300–350–400	1.5–1.2–1.0–0.9	100, 150, 200, 250, 300

This configuration proved particularly suitable for the present quartz wafers, since their thickness ($\sim$280 μm) was comparable to the depth of focus of the employed optical system ($\sim$300 μm), allowing uniform ablation throughout the entire thickness without intermediate refocusing steps. Although internal focusing could improve the final taper angle of the fabrication, it would require a short-focus objective, reducing scanning efficiency and increasing processing time. Therefore, the adopted configuration was thus chosen to balance speed and cut quality, in line with a rapid prototyping objective. Material removal was implemented by defining a milling region composed of parallel scan lines uniformly distributed across a total channel width W. The spacing between adjacent lines, denoted as the hatch distance h, was kept constant during all experiments. A hatch distance of 5 μm was selected to ensure sufficient overlap between consecutive laser passes, thereby enhancing ablation efficiency and improving cut uniformity [26, 44–46].

Based on the selected optical configuration and a measured focal spot diameter of approximately 16 μm, the degree of lateral overlap between adjacent scan lines was quantified to evaluate the effective spatial superposition of successive laser passes. The lateral overlap (LO) was calculated from the hatch spacing h and the beam radius w according to a standard geometrical relation [44]

$$LO = \left(1 - \frac{h}{2w}\right) \times 100. \tag{1}$$

Yielding an estimated overlap of 84% for the parameters employed in this study

The laser micromachining process was systematically investigated by varying four independent parameters: the laser fluence (F), the number of pulses delivered per spot (PPS), the number of repeated scanning loops (N), and the total width of the milled channel (W). The laser fluence, defined as the pulse energy density at the focal plane, was calculated from the pulse energy E and the beam radius w:

$$F = \frac{2E_P}{\pi w^2}. \tag{2}$$

The number of pulses per spot was determined by the ratio between the laser repetition rate and the scanning speed, scaled by the effective beam diameter:

$$PPS = \frac{w_0 \cdot f_R}{v} \tag{3}$$

where v is the line scanning speed.

To assess performance across the selected parameters, multiple rectangular channels were milled, each with a constant length of 3 mm and variable width (W), as depicted in figure 2(b). The corresponding sets of processing parameters used in this analysis are reported in table 1.

The investigated laser fluence F values and number of pulses were well above the multi-pulse ablation threshold of quartz [27], ensuring efficient ablation of the material already from the first processing loop.The fabricated channels were evaluated based on their depth d and taper angle θ. The latter refers to the angular deviation of the sidewalls from true perpendicularity relative to the material surface. It is typically measured as the angle formed between the sidewall of the machined feature and the vertical axis. During femtosecond laser micromachining, taper formation is a known consequence of the natural divergence of Gaussian beams, which reduces energy density with depth and leads to a narrowing, cone-like cut shape. This effect is typical of the top-down configuration. The set of laser parameters resulting in the optimal combination of high-quality cut and low taper angle was then selected for cutting quartz-based devices. The wafers were processed by tracing a milling path that matched the outer profile of the intended QTF design, as illustrated in figure 2(c). Both the milled channels and the laser-cut devices were subsequently inspected using optical (Nikon Eclipse E600) and confocal (Olympus LEXT OLS5100) microscopy. The latter was employed to reconstruct the 3D profiles of all channels thus allowing for the depths and taper angles measurements. The resonant behavior of the laser-cut QTFs was simulated via FEA using COMSOL Multiphysics. The simulation provided both the strain field distribution and the predicted fundamental resonant frequency, which was then compared with the measured values of the

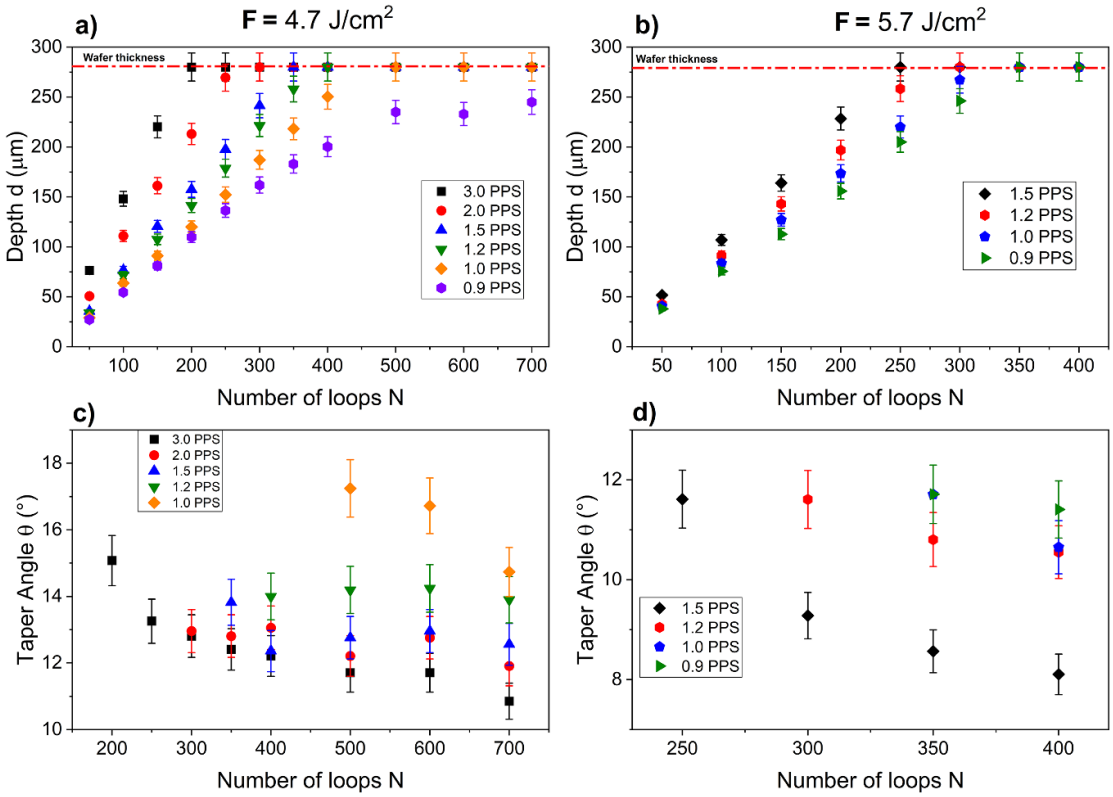

Figure 3. Depth d (a)–(b) and taper angle θ (c)–(d) measurements of the milled channels as a function of the number of loops (N), evaluated at laser fluences of 4.7 J cm^{-2} and 5.7 J cm^{-2}, with varying values of *PPS* and N.

laser-cut devices. Details of the method and experimental apparatus employed for the characterization of the resonant behavior of the laser-cut devices are reported in section 1 of the supplementary material.

3. Results and discussion

3.1. Characterization of quartz cut

The quality of the laser cut of quartz was initially assessed by evaluating the depth d and taper angle θ as a function of the laser fluence F, number of *PPS* and number of loops N. Multiple series of milled channels were fabricated with a fixed width W of 250 μm. Figures 3(a)–(d) report the trends of depth d and taper angle θ as a function of the number of loops N for varying F and *PPS* values.

Measuremen uncertainties for both depth and taper angle were estimated at 5% of the recorded values, accounting for possible deviations due to equipment precision and human handling. As shown in Figures 3(a) and 3(b), the depth (d) of the milled channels grows with increasing loop count (N) *PPS*, until it reaches the total wafer thickness (∼280 μm). Additionally, the data suggests that using higher *PPS* values enables a reduction in the minimum number of loops needed to penetrate the entire wafer. A clear linear relationship is also observed between d and the laser fluence (F): at higher F, the same depth can be attained with fewer passes and lower *PPS*. This results in distinct sets of N and *PPS* values being tested for each F setting. Notably, for $F = 4.7$ J cm^{-2}, increasing both N and *PPS* negatively impacted the cut quality, as it induced cracking throughout the quartz substrate, compromising its structural integrity.

The graphs presented in figure 3(c) and 3(d) show how the taper angle (θ) is influenced by both the number of laser passes (N) and the number of pulses applied per spot (*PPS*), under two different laser fluence (F) conditions. Only the data corresponding to channels that completely cut the wafer thickness are included. In both cases, θ tends to decrease progressively as N and *PPS* rise. Similarly, increasing F also leads to smaller taper angles. To determine the optimal processing conditions, those achieving full-depth cutting with minimal peripheral crystal damage, optical imaging was employed. In this framework, 'Front' denotes the surface where the laser initially interacts with the sample, while 'Back' identifies the opposite wafer face. Figure 4(a)–4(f) report the Front and Back facets, respectively, for six channels relevant for the quality analysis of the method.

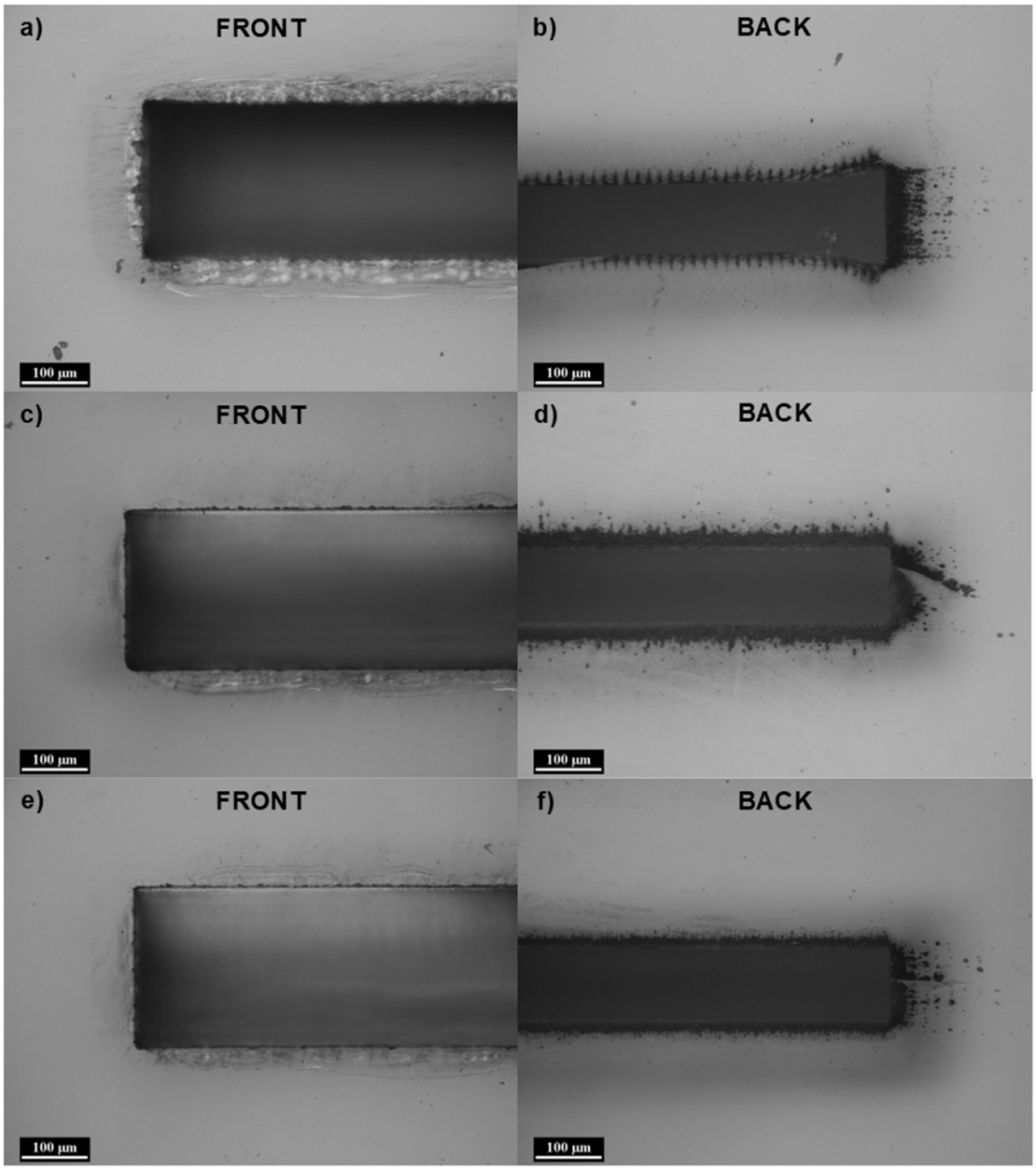

Figure 4. Images of the channel facets: (a) Front and (b) Back views corresponding to the case with $F = 5.7$ J cm^{-2}, $N = 350$, and $PPS = 0.9$. Panels (c) and (d) present Front and Back facets obtained using $F = 4.7$ J cm^{-2}, $N = 300$, and $PPS = 2$. Panels (e) and (f) show the results from the same N and energy setting as (c) and (d) but with PPS increased to 3.

Figures 4(a)–(b) corresponds to the channel obtained at $F = 5.7$ J cm^{-2}, with the lowest number of loops ($N = 350$) and the lowest PPS value (0.9), resulting in the lowest total energy deposition onto the wafer. The acquired images reveal evidence of low-quality cut. The Front facet of the channel (figure 4(a)), while not showing crack propagation, reveals significant surface alteration on both sides of the crystal, suggesting extensive crack propagation. The Back facet (figure 4(b)) exhibits an irregular shape together with the propagation of small cracks. Similar or more severe damage patterns were observed in the remaining channels processed at the same energy level. Such behavior aligns with predictions, as the higher cumulative energy, linked to elevated N and PPS settings, induces stronger stress effects in the material crystalline structure. To minimize damage and defects and ensure compatibility with the performance requirements for a QTF, this pulse energy value was not considered for cutting the final devices. Figure 4(c)–(f) reports, instead, on the two N-PPS combinations at $F = 4.7$ J cm^{-2} that resulted in minimal damage and defects. figure 4(c)–(d) and 4(e)–(f) show the Front and Back facets of the channels obtained at $F = 4.7$ J cm^{-2} with $N = 300$ & $PPS = 2$, and $N = 300$ & $PPS = 3$, respectively. Both channels show minimal crystal amorphization at the cut edges, visible only on one side, with

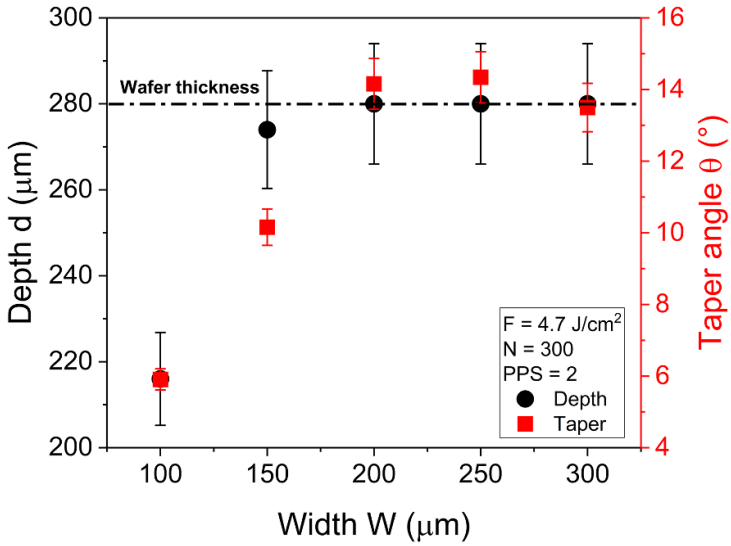

Figure 5. Measured depth d and taper angle θ values for each channel as a function of the channel width (W), obtained under fixed processing conditions: $F = 4.7$ J cm^{-2}, $N = 300$, and $PPS = 2$.

no evidence of crack propagation. The Back sides of the channels are consistent, showing regular profiles without any chipping or cracks. Among these two parameters sets, which resulted in the same taper angle ($\theta = 13° \pm 1°$), the set with $PPS = 2$ was selected due to its shorter processing time.

Using the selected parameters, a 25 mm^2 square was cut from the wafer to measure the edge roughness with a confocal microscope. A height profile was acquired along the laser-cut side wall and the resulting data were used to calculate the average roughness RA, defined as the mean absolute deviation of surface peaks and valleys from the mean line over a specific length [47]. The measurement was repeated on all four lateral walls, yielding an average roughness of $RA = 0.74 \pm 0.05$ μm. This value is in the same order of magnitude as the values reported in literature for quartz microresonators fabricated through wet etching assisted methods [48, 49].

With the selected parameters ($F = 4.7$ J cm^{-2}, $PPS = 2$ and $N = 300$), the cutting process was performed with varying widths W (see figure 2(b)). A series of five channels was fabricated with progressively increasing values of W. Cross-sectional profiles of these channels were captured using a confocal microscope and are presented in Fig. S2 of the Supplementary Material. Figure 5 reports a plot of the depth and taper angle of each of the five channels as a function of W.

Widths of 100 μm and 150 μm were found to be insufficient for the channels to fully penetrate the wafer thickness of 280 μm. Conversely, the channels realized with $W = 200$, 250, 300 μm, were able to fully cut through the wafer, each with a taper angle of around 14°, which remained consistent within the corresponding uncertainty intervals. A width of 250 μm was chosen for the QTF incision, as it ensured compatibility with both the planar (x–y) dimensions of the selected quartz tuning fork geometry (see figure 6(a)) and the thickness of the supporting substrate.

3.2. Characterization of resonant properties of the laser-cut QTFs

Quartz tuning forks were fabricated from quartz wafers using the optimized set of processing parameters ($F = 4.7$ J cm^{-2}, $PPS = 2$, $N = 300$, $W = 250$ μm), following the T-shaped configuration illustrated in figure 7(a).

The T-shaped QTF demonstrated enhanced performance for QEPAS sensing with respect to standard QTF with rectangular prongs [50]. The laser-cut QTF depicted in figure 6(b) was chosen as representative example among various similar laser-cut devices with identical geometry and shape. Prong dimensions were consistent across the fabricated devices, showing less than a 2% deviation from the nominal dimensions. A taper angle of $\theta = 13° \pm 1°$ was determined as the average value over all fabricated devices. With optimized parameters, the fabrication time for a single QTF was reduced to 30 min demonstrating the potential of this approach for rapid prototyping compared to conventional fabrication techniques.

In particular, compared to chemically assisted etching approaches reported in the literature, the proposed method offers a clear advantage in terms of prototyping throughput, as etching-based processes either require significantly longer processing times (~2 h) for wafers of comparable thicknesses [49] and

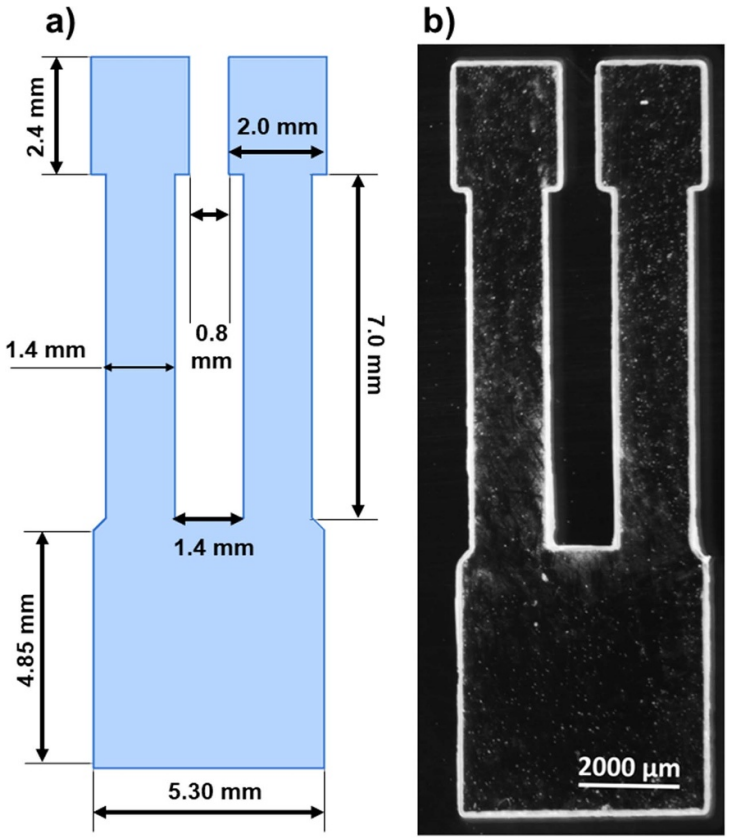

Figure 6. (a) Geometric layout of the T-shaped quartz tuning fork employed during the fabrication process.

often involve additional preliminary steps, such as laser writing and mask preparation, which further increase both the overall fabrication time [48] and production costs.To assess the vibrational response of a T-shaped quartz tuning fork, a finite element simulation was carried out using COMSOL Multiphysics (solid mechanics module). The geometry used, based on the layout in figure 6(a), included a trapezoidal cross-section with a taper of $\theta = 13°$. Figure 7 shows the resulting displacement of the prongs and the associated strain field intensity.

In addition to the strain field simulation, the tool was also used to perform an eigenfrequency analysis to predict the resonant modes of the T-shaped QTF, resulting in a resonance value of $f_0 = 11\ 079$ kHz for the fundamental antisymmetric flexural mode. This predicted frequency was subsequently taken as a reference for experimentally mapping the spectral behavior of the quartz tuning forks produced via laser cutting. The predicted value aligns closely with those measured for similar T-shaped QTFs realized though chemical etching methods [51], indicating that the taper of the prongs does not significantly affect the resonance frequency. The analysis of the strain map in figure 7 indicates a clear concentration of mechanical stress at the junction area connecting the prongs to the support. Notably, the inset reveals that the rear (Back) corner of this junction experiences a higher strain level than the front (Front) corner.

To evaluate performance, three of the various laser-cut tuning forks, identified as QTF-A, QTF-B, and QTF-C, were tested in a basic QEPAS configuration for detecting water vapor, as detailed in section 1 of the supplementary material. These QTFs were taken as representative samples, to showcase the relationship between resonant performances and quality of cut process. Their resonance profiles, corresponding to the main in-plane antisymmetric flexural mode, are shown in figure 8(a)–(c).

The vibrational response of each tuning fork was assessed by plotting prong displacement (S) versus excitation frequency (f). The experimental curves were fitted using a Lorentzian profile, with f (resonance frequency), Δf (full width at half-maximum), and S (maximum amplitude) treated as adjustable parameters. The quality factor Q was derived from the ratio between f and Δf, as defined in [52]. All relevant numerical results are compiled in table 2.

The uncertainty on S was estimated by considering the system noise, defined as the standard deviation over a 5 min acquisition of the resonance signal at peak excitation. This noise level was measured at 0.17 mV, translating into a displacement uncertainty of $\sigma = 0.001$ nm. The confidence intervals for f

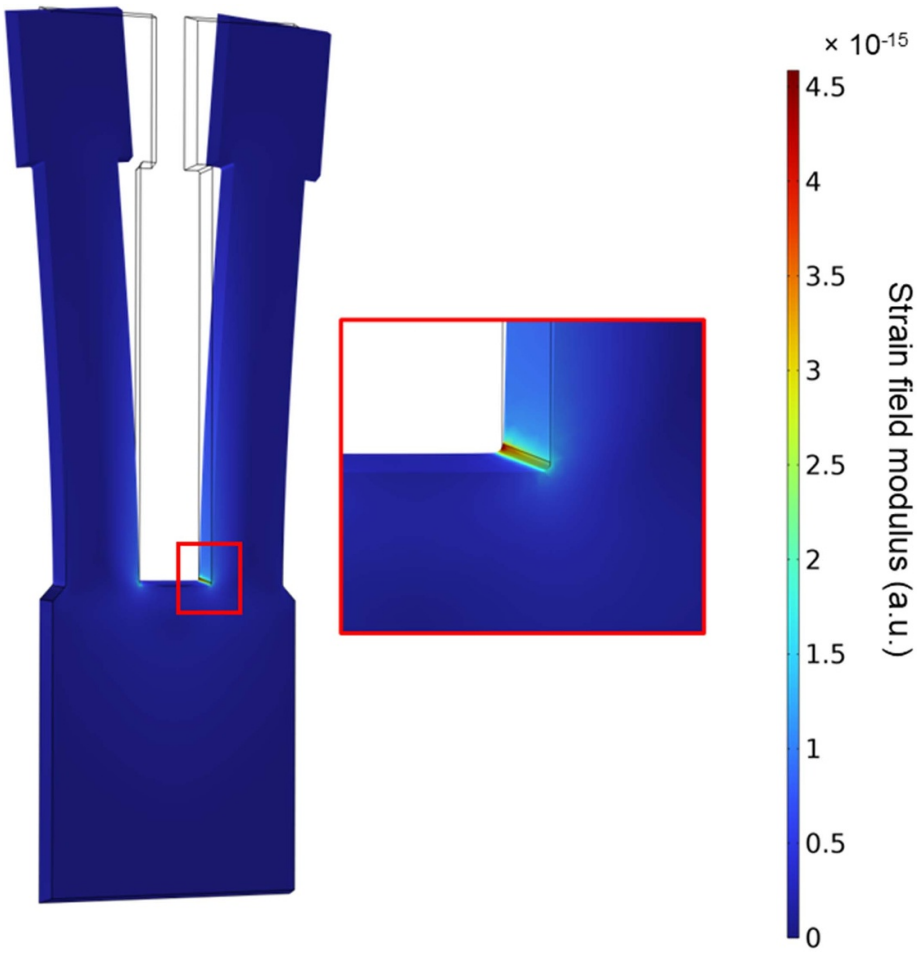

Figure 7. COMSOL-based finite element analysis showing how each prong deforms when the structure is excited in its fundamental in-plane antisymmetric flexural mode. The simulation assumes *z*-cut quartz as the material orientation. The strain field (expressed in arbitrary units) is mapped using the color scale. The inset details the area where strain is concentrated at the interface between the prongs and the base.

Table 2. Resonant properties of laser cut QTFs from Lorentzian function fitting analysis.

QTF	f_0 [Hz]	Δf [Hz]	S_{peak} [nm]	Q
QTF-A	11 095.20 ± 0.01	1.40 ± 0.01	0.140 ± 0.001	7900 ± 56
QTF-B	10 958.20 ± 0.01	1.59 ± 0.01	0.120 ± 0.001	6900 ± 43
QTF-C	10 897.00 ± 0.01	1.94 ± 0.02	0.100 ± 0.001	5600 ± 59
SIMULATED	11 079	N.A.	N.A.	N.A.

and Δf were directly extracted from the curve-fitting process, while the corresponding error on Q was computed through propagation, using the relation $Q = f/\Delta f$. The experimentally observed resonance frequencies were found to closely match the value of $f_0 = 11\ 079$ kHz predicted from the eigenfrequency study, with a maximum deviation not exceeding 2% [9]. A clear and significant difference in the quality factor (Q) is observed among the three examined QTFs. In particular, QTF-A exhibits a Q value that surpasses those of QTF-B and QTF-C by approximately 13% and 30%, respectively. Since all devices share nearly identical resonance frequencies (f_0), the data in table 2 suggest that such differences are likely attributable to variations in fabrication quality, with particular emphasis on the precision of the cutting process.

The prong-to-support junction emerges as a crucial region for two main reasons: (i) simulation results show this area experiences the highest concentration of mechanical strain, and (ii) it functions as a primary channel for vibrational energy dissipation, contributing significantly to support-related losses. The presence of structural imperfections—such as microcracks—affecting the integrity of the crystal bulk in this region can therefore enhance energy dissipation [53], resulting in a diminished Q and a disturbed strain distribution, as depicted in figure 7.

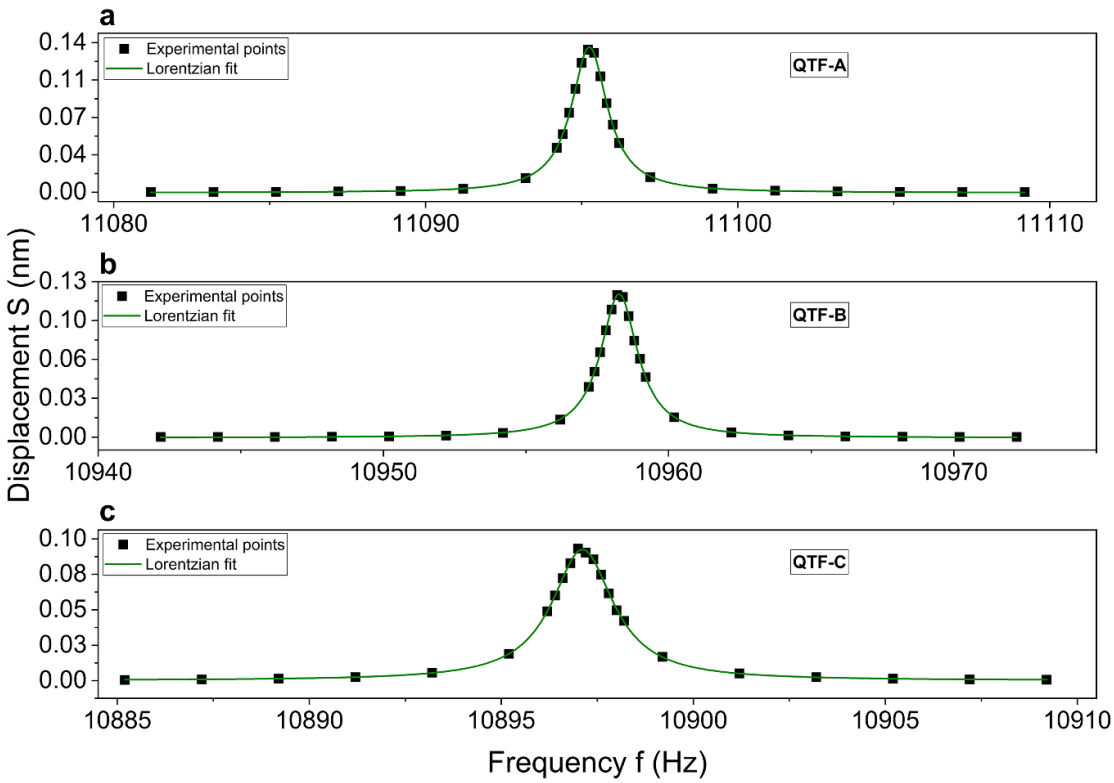

Figure 8. Experimentally acquired resonance profiles for QTF-A, QTF-B, and QTF-C, shown in panels (a), (b), and (c), respectively. Each dataset has been fitted using a Lorentzian function (green line) to extract the resonance parameters.

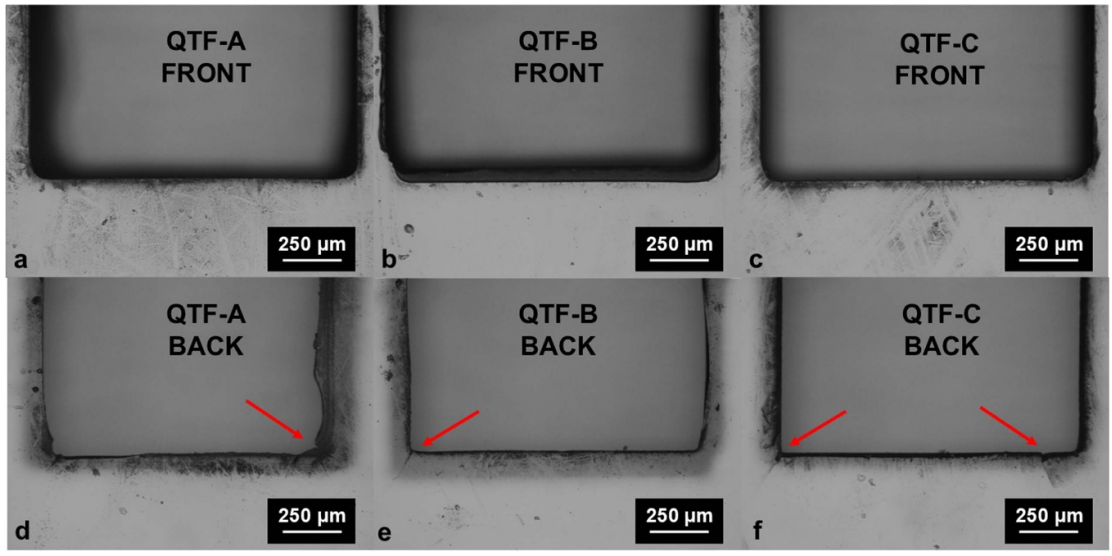

Figure 9. Optical images showing the front facets of the prong-support junctions for QTF-A, QTF-B, and QTF-C are displayed in panels (a), (b), and (c), respectively. Corresponding images of the back facets are shown in panels (d), (e), and (f). Red arrows highlight the presence of micro-defects or fine cracks observed at the junction regions.

Figures 9(a)–(f) presents comparative images of the front and rear facets at the prong-support interface for QTF-A, QTF-B, and QTF-C.

Figures 9 (a)–(c) display the front facets of the prong-support junctions for QTF-A, QTF-B, and QTF-C, respectively. All three devices exhibit comparable quality in this region, with no visible defects at the corners where the prongs connect to the support structure. In contrast, the back facets shown in figure 9(d)–(f) reveal varying degrees of crystal damage. Specifically, QTF-B (figure 9(e)) and QTF-C (figure 9(f) exhibit clearly visible cracks at the junction corners, while QTF-A (figure 9(d)) shows only a

faint and barely noticeable defect. QTF-C presents the most severe damage, with one crack observed at each corner.

A strong correlation is evident between the extent of these structural imperfections, affecting the bulk crystal structure, and the quality factor values reported in table 2. QTF-C, affected by two distinct cracks, exhibits the lowest Q value (5600), followed by QTF-B, which shows a single crack and a Q of 6900. QTF-A, with only a minor defect, achieves the highest Q value (7900). A comparison with Q-factor values of the order of 12 000, reported for QTFs fabricated using standard etching techniques for the same geometry [54], highlights the critical role of crystal bulk integrity, particularly at the prong–support junction, in determining the resonance performance of laser-cut QTFs. This region is identified as the main factor currently limiting the Q-factor of the fabricated prototypes. Consequently, improving the quality of the laser cut in the prong–body junction region represents a key objective for future developments of the proposed fabrication process. Furthermore, the observed correlation between cracks and Q-values confirms that the taper angle and minor superficial irregularities in the micromachined edges do not impact device performance, since they have no impact on bulk integrity. The same conclusion can be drawn relatively to the sidewall surface roughness since the three QTFs have all sidewall R_A values which are within the uncertainty interval of the average R_A reported above. If these factors had been significant, QTF-A, which exhibited a slightly irregular profile at the lower back end of its right prong, would have displayed a lower Q-value compared to QTF-B and QTF-C.

Section 3 of the Supplementary Materials reports on the mapping of the QTF prong displacement and proof-of-operation of the laser-cut devices in a QEPAS apparatus for the detection of ambient water vapor.

4. Conclusions

This study demonstrated a reliable and efficient method for the direct fabrication of QTFs using femtosecond laser micromachining, establishing a viable alternative to conventional chemical etching techniques. The approach employed a femtosecond laser system operating at a wavelength of 515 nm and combined a milling channel technique with a top–bottom processing configuration. This strategy enabled clean, precise cuts through quartz wafers up to 280 μm thick—consistent with the standard dimensions used in QTF manufacturing—while allowing for high tunability and reproducibility.

The fabricated QTFs featured T-shaped prongs with a trapezoidal cross-section, a consequence of the tapering introduced by the top-side processing approach. Finite element simulations incorporated this geometry to predict the resonance frequency of the fundamental in-plane antisymmetric flexural mode. Experimental evaluation of three laser-machined QTFs yielded resonance frequencies within 2% of the simulated reference value (11079 Hz). Variations in the measured quality factors (5600, 6900, and 7900) were attributed to differences in the structural integrity at the back corners of the prong-support junctions, confirming the critical role of localized defects in determining device performance.

These results highlight femtosecond laser processing as a flexible, scalable, and environmentally sustainable approach for producing micro-resonator QTFs. This technique is particularly advantageous for developing innovative designs in the prototyping phase, offering precision and adaptability unmatched by traditional methods.

Data availability statement

All data that support the findings of this study are included within the article (and any supplementary files).

Setup for QTFs characterization available at https://doi.org/10.1088/2515-7647/ae3505/data1.
Channel width characterization available at https://doi.org/10.1088/2515-7647/ae3505/data2.
QTFs prong displacements available at https://doi.org/10.1088/2515-7647/ae3505/data3.
Water feature spectral scan available at https://doi.org/10.1088/2515-7647/ae3505/data4.

Funding Statement

The authors from Dipartimento Interuniversitario di Fisica di Bari acknowledge financial support from PNRR MUR project PE0000023-NQSTI, project MUR—Dipartimenti di Eccellenza 2023–2027—Quantum Sensing and Modelling for One-Health (QuaSiModO), PRIN 2022 PNRR Project 'Surface and Interface acoustic wave-driven Microfluidic devices BAsed on fs-laser technology for particle sorting (SIMBA)' (grant number: Prot. P2022LMRKB) and THORLABS GmbH within the PolySenSe joint research laboratory.

Author contributions

Raffaele De Palo 0000-0002-3563-2206
Conceptualization (equal), Data curation (equal), Formal analysis (equal), Methodology (equal), Validation (equal), Writing – original draft (equal), Writing – review & editing (equal)

Jaka Mur 0000-0001-9317-9836
Conceptualization (equal), Methodology (equal), Resources (equal), Visualization (equal), Writing – review & editing (equal)

Matevž Marš 0009-0005-6891-3839
Investigation (equal), Resources (equal)

Felice Alberto Sfregola 0009-0007-7775-9970
Software (equal), Visualization (equal), Writing – review & editing (equal)

Pietro Patimisco
Conceptualization (equal), Funding acquisition (equal), Methodology (equal), Resources (equal), Supervision (equal), Writing – review & editing (equal)

Vincenzo Spagnolo 0000-0002-4867-8166
Funding acquisition (equal), Resources (equal), Supervision (equal), Writing – review & editing (equal)

Antonio Ancona
Resources (equal), Writing – review & editing (equal)

Rok Petkovšek
Resources (equal), Supervision (equal), Writing – review & editing (equal)

Annalisa Volpe
Conceptualization (equal), Funding acquisition (equal), Methodology (equal), Resources (equal), Supervision (equal), Visualization (equal), Writing – review & editing (equal)

References

[1] Anderson R S and Anderson S P 2010 *Geomorphology: The Mechanics and Chemistry of Landscapes* (Cambridge University Press)
[2] Kihara K 1990 An x-ray study of the temperature dependence of the quartz structure *Eur. J. Mineral.* **2** 63–78
[3] Saigusa Y 2017 *Advanced Piezoelectric Materials* 2nd edn, ed K Uchino (Elsevier) pp 197–233
[4] Calabrese E et.al 1978 Electronic energy-band structure of α quartz *Phys. Rev. B* **18** 2888
[5] Babaei M H and Chen Z T 2009 Dynamic response of a thermopiezoelectric rod due to a moving heat source *Smart Mater Struct.* **18** 025003
[6] Speight R E and Cooper M A 2012 A Survey of the 2010 quartz crystal microbalance literature *J. Mol. Recognit.* **25** 451–73
[7] Kosterev A A, Tittel F K, Serebryakov D V, Malinovsky A L and Morozov I V 2005 Applications of quartz tuning forks in spectroscopic gas sensing *Rev. Sci. Instrum.* 76
[8] De Palo R, Volpe A, Patimisco P, Zifarelli A, Sampaolo A, Ancona A, Wu H and Spagnolo V 2025 Femtosecond laser fabrication of black quartz for infrared photodetection applications *Light Adv. Manuf.* **6** 1
[9] Patimisco P, Sampaolo A, Zheng H, Dong L, Tittel F K and Spagnolo V **2**017 Quartz–enhanced photoacoustic spectrophones exploiting custom tuning forks: a review *Adv. Phys.* **2** 641–74
[10] Yuan J-Q, Zhao B, Sun L-S, Wu L-T, Guo T-J, Kang M and Chen J 2021 Optical super-resonance in a customized P T -symmetric system of hybrid interaction *Opt. Mater. Express* **29** 24663
[11] Classification P and Klein J L 2006 (*12) Patent Application Publication (10) Pub. No.:* US 2006/0196845 A11
[12] Lin H *et al* 2023 Application of standard and custom quartz tuning forks for quartz-enhanced photoacoustic spectroscopy gas sensing *Appl. Spectrosc. Rev.* **58** 562–84
[13] Yeh M-P, Wu L-F, Fan E-T, Chen T, Chuang T-S, Lee S L and Tung K-L 2024 Characteristics of inorganic acid emission from various generation semiconductor manufacturing factories *Chemosphere* **347** 140745
[14] Gamaly E G, Rode A V and Luther-Davies B 2002 Ablation of solids by femtosecond lasers: ablation mechanism and ablation thresholds for metals and dielectrics *Phys. Plasmas* **9** 949
[15] Gaudiuso C 2023 Laser fabrication: a solid present for the brightest future *Appl. Sci.* **13** 10831
[16] Ouchene A, Mollon G, Ollivier M, Sedao X, Pascale-Hamri A, Dumazer G and Serris E 2023 Roughness and wettability control of soda-lime silica glass surfaces by femtosecond laser texturing and curing environments *Appl. Surf. Sci.* **630** 157490
[17] Yan S, Wei C, Zou H, Chen J, Li Y, Shen T, Wang A, Sui T and Lin B 2021 Fabrication and tribological characterization of laser textured engineering ceramics: si3N4 SiC and ZrO2 *Ceram. Int.* **47** 13789–805
[18] Dkhar D S, Kumari R, Malode S J, Shetti N P and Chandra P 2023 Integrated lab-on-a-chip devices: fabrication methodologies, transduction system for sensing purposes *J. Pharm. Biomed. Anal.* **223** 115120
[19] Fan Z, Cui D, Zhang Z, Zhao Z, Chen H, Fan Y, Li P, Zhang Z, Xue C and Yan S 2021 Recent progress of black silicon: from fabrications to applications *Nanomaterials* **11** 41

[20] Sfregola F A, De Palo R, Gaudiuso C, Patimisco P, Ancona A and Volpe A 2024 Femtosecond laser transmission joining of fused silica and polymethyl methacrylate *Macromol. Mater. Eng.* **310** 2400354
[21] Radhakrishnan J, Scott R and Marimuthu S 2025 Precision machining of alumina-reinforced ceramic matrix composites by femtosecond laser *Int. J. Adv. Manuf. Technol.* **138** 1335–48
[22] Shin H and Kim D 2018 Cutting thin glass by femtosecond laser ablation *Opt. Laser Technol.* **102** 1–11
[23] Shin H, Noh J and Kim D 2021 Bottom-up cutting method to maximize edge strength in femtosecond laser ablation cutting of ultra-thin glass *Opt. Laser Technol.* **138** 106921
[24] Yadav A, Kbashi H, Kolpakov S, Gordon N, Zhou K and Rafailov E U 2017 Stealth dicing of sapphire wafers with near infra-red femtosecond pulses *Appl. Phys. A* **123** 1–7
[25] Ashkenasi D, Lorenz M, Stoian R and Rosenfeld A 1999 Surface damage threshold and structuring of dielectrics using femtosecond laser pulses: the role of incubation *Appl. Surf. Sci.* **150** 101–6
[26] Ben-Yakar A et.al 2004 Femtosecond laser ablation properties of borosilicate glass *J. Appl. Phys.* **96** 5316–23
[27] De Palo R, Volpe A, Gaudiuso C, Patimisco P, Spagnolo V and Ancona A 2022 Threshold fluence and incubation during multi-pulse ultrafast laser ablation of quartz *Opt. Mater. Express* **30** 44908
[28] Eberle G, Schmidt M, Pude F and Wegener K 2016 Laser surface and subsurface modification of sapphire using femtosecond pulses *Appl. Surf. Sci.* **378** 504–12
[29] Han J, Malek O, Vleugels J, Braem A and Castagne S 2022 Ultrashort pulsed laser ablation of zirconia-alumina composites for implant applications *J. Mater. Process. Technol.* **299** 117335
[30] Bonse J, Höhm S, Kirner S V, Rosenfeld A and Krüger J 2017 Laser-induced periodic surface structures-A scientific evergreen *IEEE J. Sel. Top. Quantum Electron.* **23** 1–15
[31] Lapointe J, Bérubé J-P, Ledemi Y, Dupont A, Fortin V, Messaddeq Y and Vallée R 2020 Nonlinear increase, invisibility, and sign inversion of a localized fs-laser-induced refractive index change in crystals and glasses *Light: Sci. Appl.* **9** 64
[32] Costache F, Eckert S and Reif J 2008 Near-damage threshold femtosecond laser irradiation of dielectric surfaces: desorbed ion kinetics and defect dynamics *Appl. Phys. A* **92** 897–902
[33] Li Z-Z, Fan H, Wang L, Zhang X, Zhao X-J, Yu Y-H, Xu Y-S, Wang Y, Wang X-J and Juodkazis S 2024 Super-stealth dicing of transparent solids with nanometric precision *Nat. Photon.* 1–10
[34] Quzwain K, Ismail A and Sali A 2017 Octagon fractal microstrip Yagi antenna with a combined DNG and DPS layer structure *Microw. Opt. Technol. Lett.* **59** 1988–93
[35] Teh W H, Boning D S and Welsch R E 2015 Multi-strata stealth dicing before grinding for singulation-defects elimination and die strength enhancement experiment and simulation *IEEE Trans. Semicond. Manuf.* **28** 408–23
[36] Meyer R, Rapp L, Safioui J, Furfaro L, Dudley J M and Courvoisier F 2016 Stealth dicing with Bessel beams and beyond *Optics InfoBase Conf. Papers*
[37] Dudutis J, Stonys R, Račiukaitis G and Gečys P 2018 Bessel beam asymmetry control for glass dicing applications *Procedia CIRP* **74** 333–8
[38] Gaudiuso C, Volpe A and Ancona A 2020 One-step femtosecond laser stealth dicing of quartz *Micromachines* **11** 327
[39] Wang Y, Dai Y, Mumtaz F and Luo K 2024 Advanced techniques in quartz wafer precision processing: stealth dicing based on filament-induced laser machining *Opt. Laser Technol.* **171** 110474
[40] Wang Y, Mumtaz F and Dai Y 2023 Micromachining of SiO_2 single crystal wafer using femtosecond laser *J. Laser Appl.* **35** 022004
[41] Černe L, Petelin J and Petkovšek R 2020 Femtosecond CPA hybrid laser system with pulse-on-demand operation *Opt. Mater. Express* **28** 7875–88
[42] Černe L and Šušnjar P 2021 Compensation of optical nonlinearities in a femtosecond laser system in a broad operation regime *Opt. Laser Technol.* **135** 106706
[43] Wlodarczyk K L, Brunton A, Rumsby P and Hand D P 2016 Picosecond laser cutting and drilling of thin flex glass *Opt. Lasers Eng.* **78** 64–74
[44] Sfregola F A et.al 2024 Influence of working parameters on multi-shot femtosecond laser surface ablation of lithium niobate *Opt. Laser Technol.* **177** 111067
[45] Gamaly E G, Rode A V, Perrone A and Zocco A 2001 Mechanisms of ablation-rate decrease in multiple-pulse laser ablation *Appl. Phys. A* **73** 143–9
[46] Byskov-Nielsen J, Savolainen J-M, Christensen M S and Balling P 2010 Ultra-short pulse laser ablation of metals: threshold fluence incubation coefficient and ablation rates *Appl. Phys. A* **101** 97–101
[47] Taufik M et.al 2016 A study of build edge profile for prediction of surface roughness in fused deposition modeling *J. Manuf. Sci. Eng.* **138** 061002
[48] Ma W, Yu X, Wang R, Tian F, Tang Z, Zhang Z, Qiu L, Shang K, Xu K and Zhao W 2025 Efficient fabrication of high-quality quartz pendulous via femtosecond laser bessel beams writing-enhanced wet etching *Opt. Commun.* **587** 131896
[49] Xue H, Ai J, Zhang Z, Li B, Bai B, Li C and Zhao Y 2025 Deep wet etching of a z-cut α-quartz wafer by fluorine-based solutions: experiment *J. Microelectromech. Syst.* **34** 332–46
[50] Patimisco P, Sampaolo A, Giglio M, Dello Russo S, Mackowiak V, Rossmadl H, Cable A, Tittel F K and Spagnolo V 2019 Tuning forks with optimized geometries for quartz-enhanced photoacoustic spectroscopy *Opt. Mater. Express* **27** 1401–15
[51] Sampaolo A, Patimisco P, Giglio M, Zifarelli A, Wu H, Dong L and Spagnolo V 2022 Quartz-enhanced photoacoustic spectroscopy for multi-gas detection: a review *Anal. Chim. Acta* **1202** 338894
[52] Patimisco P, Sampaolo A, Dong L, Giglio M, Scamarcio G, Tittel F K and Spagnolo V 2016 Analysis of the electro-elastic properties of custom quartz tuning forks for optoacoustic gas sensing *Sens. Actuators B* **227** 539–46
[53] Hao Z, Erbil A and Ayazi F 2003 An analytical model for support loss in micromachined beam resonators with in-plane flexural vibrations *Sens. Actuators A* **109** 156–64
[54] Olivieri M, Zifarelli A, Menduni G, Di Gioia M, Marzocca C, Passaro V M N, Sampaolo A, Giglio M, Spagnolo V and Patimisco P 2021 Influence of air pressure on the resonance properties of a t-shaped quartz tuning fork coupled with resonator tubes *Appl. Sci.* **11** 7974